

## RESEARCH ARTICLE

View Article Online

View Journal | View Issue

Cite this: *Inorg. Chem. Front.*, 2023, **10**, 1614Solvent-controlled synthesis of an  $\text{Al}_{12}$ -oxo molecular ring and  $\text{Al}_{24}$ -oxo truncated metallo-cube†

Ying Zou, Wei Lv, Zhen-Zhen Xue, Jin-Hua Li, Xiao-Yu Li \* and Guo-Ming Wang \*

Highly symmetrical molecules with beautiful geometries are ubiquitous in nature. It has inspired creative ideas of the perfect combination of geometry and molecular structural chemistry. Some metal clusters with regular geometric polyhedra have been reported, but such highly symmetric polyhedra for Al-oxo clusters are really scarce on account of the fast hydrolysis of  $\text{Al}^{3+}$  ions. Herein, a  $[\text{Al}_{12}(\text{CH}_3\text{O})_{24}(\text{NAP})_{12}] \cdot 4\text{DMF} \cdot 2\text{H}_2\text{O} \cdot 2\text{CH}_3\text{OH}$  (**Al<sub>12</sub>**,  $\text{NAP}^- = 2$ -naphthoic acid) nanoring was synthesized by the solvothermal reaction of  $\text{AlCl}_3 \cdot 6\text{H}_2\text{O}$ , 2-naphthoformic acid (HNAP) and triethylamine ( $\text{Et}_3\text{N}$ ) in  $\text{CH}_3\text{OH}$  and DMF. Interestingly, the regulation from ring-shaped **Al<sub>12</sub>** to  $[\text{Al}_{24}(\text{OH})_{32}(\text{CH}_3\text{O})_{22}(\text{CH}_3\text{OH})_2(\text{NAP})_{12}] \cdot 6\text{Cl} \cdot 2\text{H}_2\text{O} \cdot 2\text{CH}_3\text{OH}$  (**Al<sub>24</sub>**) metallogage is realized by only changing the reactive solvents. The **Al<sub>24</sub>** metallogage can be seen as one of 13 Archimedean polyhedra, a truncated cube composed of eight  $\text{Al}_3$  triangles and six  $\text{Al}_8$  octagons by sharing vertical  $\text{Al}^{3+}$  ions. In addition, high-resolution electrospray ionization mass spectrometry (HR-ESI-MS) reveals that the metallic skeletons of **Al<sub>12</sub>** and **Al<sub>24</sub>** can be maintained stable in  $\text{CH}_3\text{OH}$  and  $\text{CH}_2\text{Cl}_2$ . Furthermore, **Al<sub>12</sub>** and **Al<sub>24</sub>** emit blue luminescence and exhibit photocurrent responses under LED light illumination.

Received 21st November 2022,

Accepted 27th January 2023

DOI: 10.1039/d2qi02461f

rsc.li/frontiers-inorganic

## Introduction

Highly symmetrical polyhedra have intrigued various professional researchers in the fields of mathematics, biology, aesthetics, architecture, and chemistry for thousands of years.<sup>1–6</sup> The classical polyhedra contain 5 platonic polyhedra constructed by one kind of regular convex polygon with the same number of faces at each vertex, and 13 Archimedean polyhedra composed of two or more types of regular polygons.<sup>7</sup> In chemistry, these exemplifications have been found in coordination molecular nanocages and nanoclusters of coordination chemistry.<sup>8</sup> For coordination nanocages, based on the construction rules of polyhedra, suitable organic ligands with specific configurations are often selected for their syntheses.<sup>9–14</sup> However, the nanoclusters assembled from simple ingredients are elusive and the acquisition of geometric structures lacks the presupposition. As a famous polyhedral cluster,  $\text{C}_{60}$  is constructed by 12 pentagons and 20 hexagons, which is a classical Archimedean polyhedron, truncated icosahedron, inspiring various creative ideas for building fullerene-like nanopolyhedral metal clusters.<sup>15</sup> After long-term unremitting efforts, tran-

sition/lanthanide metal clusters with Platonic and Archimedean polyhedra have been isolated, such as  $\text{V}_{24}$ ,<sup>16</sup>  $\text{Co}_{32}$ ,<sup>17</sup>  $\text{Cd}_{66}$ ,<sup>18</sup>  $\text{Mo}_{240}$ ,<sup>19</sup>  $\text{Pd}_{145}$ ,<sup>20</sup>  $\text{Ag}_{180}$ ,<sup>21</sup> and  $\text{Ln}_{104}$ .<sup>22</sup>

As the most abundant metal element in the earth's crust, Al clusters with lightweight and high stability have potential applications in environmental science, geochemistry, biology, optical, and adsorption materials.<sup>23,24</sup> Aqueous aluminum chemistry presents a series of typical aluminum oxo-hydroxo polycation aggregations, as exemplified by flat- $\text{Al}_{13}$   $[\text{Al}_{13}(\text{OH})_{24}(\text{H}_2\text{O})_{24}]^{15+}$ ,<sup>25,26</sup> isomers of the  $\text{Al}_{13}$ -Keggin cluster  $[\text{Al}_{13}\text{O}_4(\text{OH})_{24}(\text{H}_2\text{O})_{12}]^{7+}$ ,<sup>24,27</sup> and larger  $\text{Al}_{30}$  clusters  $[\text{Al}_{30}\text{O}_8(\text{OH})_{56}(\text{H}_2\text{O})_{26}]^{18+}$ .<sup>24,28</sup> They were produced from hydrolytic processes of  $\text{Al}^{3+}$  ions in aqueous solutions, which is actually intricate and affected by ololation reactions, formation of precursors, aggregation, nucleation and crystallization.<sup>24,27</sup> An effective route is to choose suitable trapping ligands, such as  $\text{Al}_3$  and  $\text{Al}_8$  protected by the trisilanol ligand,<sup>29</sup> a supramolecular zeotype  $\text{Al}_{15}$  constructed using hpdta ( $\text{H}_5\text{hpdta} = \text{HOCH}_2[\text{CH}_2\text{N}(\text{CH}_2\text{COOH})_2]_2$ ).<sup>30</sup> Although many efforts have been made to investigate the aqueous aluminum chemistry of hydrolysis and polymerization of  $\text{Al}^{3+}$  ions, the relationship of solution equilibria and the existence of polynuclear species is still complex and unpredictable.<sup>31</sup> For this dilemma, recently, a new strategy known as coordination delayed hydrolysis has been adopted by Zhang *et al.* to synthesize a series of Al-oxo clusters by choosing monodentate carboxylic acid ligands and organic aluminium salts under solvothermal conditions.<sup>32–35</sup>

College of Chemistry and Chemical Engineering, Qingdao University, Shandong 266071, China. E-mail: xylichem@qdu.edu.cn, gmwang\_pub@163.com

†Electronic supplementary information (ESI) available. CCDC 2163632 and 2163633. For ESI and crystallographic data in CIF or other electronic format see DOI: <https://doi.org/10.1039/d2qi02461f>

Most of these Al-oxo clusters feature the structures of molecular rings from  $\text{Al}_8$  to the largest  $\text{Al}_{20}$  constructed using different large conjugated carboxylic acids.<sup>33,34,36</sup> The different peripheral ligands realize luminescence modulation of  $\text{Al}_{20}$  molecular rings from blue to green. Besides, other Al clusters also display luminescence properties, which originated from the luminescence of the corresponding ligands.<sup>37</sup> Nevertheless, highly symmetric aluminum-oxo clusters are rare because of the rapid hydrolysis of  $\text{Al}^{3+}$  ions and the difficult precipitation of high-quality and determinable single crystals.<sup>36</sup> Many efforts will be made to further explore the assembly and luminescence properties of aluminum-oxo clusters.

Based on these considerations, enlightened by the simple one-pot solvothermal synthesis method of transition/lanthanide metal clusters accompanied by adding alkali to control the hydrolysis of metal ions, a ring  $\text{Al}_{12}$  dodecagon with the formula,  $[\text{Al}_{12}(\text{CH}_3\text{O})_{24}(\text{NAP})_{12}] \cdot 4\text{DMF} \cdot 2\text{H}_2\text{O} \cdot 2\text{CH}_3\text{OH}$  was obtained in  $\text{CH}_3\text{OH}$ -DMF by the reaction of monodentate carboxylic acid and inorganic aluminium salt with  $\text{Et}_3\text{N}$  to adjust the alkalinity of the solution. When using  $\text{CH}_3\text{OH}$ - $\text{CH}_3\text{CN}$  as the solvent, a new Archimedean polyhedron  $\text{Al}_{24}$ ,  $[\text{Al}_{24}(\text{OH})_{32}(\text{CH}_3\text{O})_{22}(\text{CH}_3\text{OH})_2(\text{NAP})_{12}] \cdot 6\text{Cl} \cdot 2\text{H}_2\text{O} \cdot 2\text{CH}_3\text{OH}$  was isolated. It features a truncated-cube metallocage containing 8  $\text{Al}_3$  triangles and 6  $\text{Al}_8$  octagons. This work successfully realizes the regulation of Al-oxo skeletons from molecular ring to metallocage. Moreover, the metallic cores of  $\text{Al}_{12}$  and  $\text{Al}_{24}$  have good stability in methanol and dichloromethane with the ligand exchange. Furthermore, the photocurrent response and the temperature-responsive luminescence behaviour of the  $\text{Al}_{12}$  and  $\text{Al}_{24}$  were investigated.

## Experimental

### Materials and physical measurements

Chemicals and solvents were purchased without further purification. On an ABB Bomen MB 102 series FT-IR (KBr pellets) spectrometer, IR spectra were recorded in the 4000–400  $\text{cm}^{-1}$  region. The elemental analyses were conducted on a Vario EL cube analyzer. Powder X-ray diffraction (PXRD) data were obtained on the Rigaku SmartLab X-ray diffractometer. Thermogravimetric (TG) curves were measured from ambient temperature to 800 °C using the SDT Q600 analyzer. A Puxi Tu-1901 spectrophotometer was used to measure UV-vis spectra. A Bruker Impact II high-definition mass spectrometer quadrupole and time-of-flight (Q/TOF) modules were used to record the mass spectra (HR-ESI-MS). The photocurrent experiments were performed on a CHI660E electrochemistry workstation. The 10 L of naphthol (0.5 wt%) and 5 mg samples of  $\text{Al}_{12}$  or  $\text{Al}_{24}$  were combined with 0.5 mL of ethanol and then subjected to a 30-minute sonication process. The coated film was produced by pipetting 150  $\mu\text{L}$  solution onto the cleaned ITO glass after evaporation. A Pt wire served as the counter electrode, an Ag/AgCl electrode served as the reference electrode, and the produced ITO glass film served as the working electrode. The medium was an aqueous solution of  $\text{Na}_2\text{SO}_4$  (0.2 M). An

F-4700 fluorescence spectrometer was used to measure the room-temperature fluorescence. The Edinburgh spectrofluorometer (FLS980), with a cryostat to regulate temperature, was used to collect variable-temperature fluorescence data. After a 10-minute homeothermy, each data was collected and quantum yield data were obtained on the integrating sphere, and the luminescence lifetimes were determined on the same device using a time-correlated single-photon counting method (FLS980).

### Synthesis of $\text{Al}_{24}$

A mixture of 2-naphthoformic acid (HNAP, 172.2 mg, 1 mmol),  $\text{AlCl}_3 \cdot 6\text{H}_2\text{O}$  (500 mg, 2 mmol), were dissolved in a mixed solvent of  $\text{CH}_3\text{OH}$  (3 mL): $\text{CH}_3\text{CN}$  (8 mL) in a 23 mL Teflon-lined reaction vessel, then 0.5 mL triethylamine ( $\text{Et}_3\text{N}$ ) were added into the mixture under stirring, finally kept at 100 °C for 4 days. When slowly cooled to room temperature, washed with  $\text{CH}_3\text{OH}$ , and dried in the air, colorless block crystals were obtained (yield 35.62% based on  $\text{AlCl}_3 \cdot 6\text{H}_2\text{O}$ ). Elemental analyses calcd. (found) for  $\text{Al}_{24}$ :  $\text{C}_{158}\text{H}_{202}\text{Al}_{24}\text{Cl}_6\text{O}_{84}$ : C, 44.08 (43.89); H, 4.73 (4.92)%. Selected IR peaks ( $\text{cm}^{-1}$ ): 3450 (s), 3060 (w), 2950 (m), 2840 (w), 2670 (w), 1610 (s), 1570 (m), 1480 (s), 1430 (s), 1070 (m), 982 (m), 870 (m), 796 (s), 594 (s), 501 (w).

### Synthesis of $\text{Al}_{12}$

The  $\text{Al}_{12}$  is similar to  $\text{Al}_{24}$  except for  $\text{CH}_3\text{OH}:\text{CH}_3\text{CN}$  (11 mL, v:v = 3:8) was replaced by  $\text{CH}_3\text{OH}$  and DMF (10 mL, v:v = 1:1), colorless lamellar crystals were obtained (yield 40.56% based on  $\text{AlCl}_3 \cdot 6\text{H}_2\text{O}$ ). Elemental analyses calcd. (found) for  $\text{Al}_{12}$ :  $\text{C}_{170}\text{H}_{196}\text{Al}_{12}\text{N}_4\text{O}_{56}$ : C, 58.09 (57.87); H, 5.62 (5.78); N, 1.59 (1.62)%. Selected IR peaks ( $\text{cm}^{-1}$ ): 3434 (s), 2964 (m), 2925 (m), 2856 (m), 2296 (w), 1629 (s), 1381 (m), 1080 (m), 1043 (m), 929 (w), 879 (w), 565 (w).

### X-ray crystallography

Single crystals of  $\text{Al}_{24}$  and  $\text{Al}_{12}$  with the appropriate dimensions were selected under an optical microscope, coated fast into high vacuum grease, and put on a glass fiber for single-crystal data collection with Cu K $\alpha$  radiation on the Rigaku XtaLAB MM007 CCD diffractometer. OLEX<sup>38</sup> and SHELXL-97 were used to directly solve the structures.<sup>39</sup> Based on the relevant atoms and refined with predetermined temperature factors, all hydrogen atoms were theoretically hydrogenated. To ensure that no extra symmetry could be given to the models, the Addsym function of PLATON<sup>40</sup> was used to check each structure. The SQUEEZE command was used to eliminate the disorganized solvent molecules. The Cambridge Crystallographic Data Centre (CCDC) has received the crystallographic information from this article (CCDC: 2163632 ( $\text{Al}_{12}$ ); 2163633 ( $\text{Al}_{24}$ )).<sup>†</sup> Table S6<sup>†</sup> provides the pertinent crystallographic data. Table S7<sup>†</sup> displays the selected bond lengths and angles.

## Results and discussion

### Crystal structure of $\text{Al}_{12}$ cluster

Single-crystal X-ray diffraction analysis revealed that the  $\text{Al}_{12}$  cluster crystallizes in the triclinic  $P\bar{1}$  space group and it contains 12  $\text{Al}^{3+}$ , 12  $\text{NAP}^-$ , and 24  $\text{CH}_3\text{O}^-$  (Fig. 1a). Twelve  $\text{Al}^{3+}$  ions form a complanate dodecagon with the Al–Al distances in the range of 2.8621–2.8781 Å and every  $\text{Al}^{3+}$  ion is located on the vertex of a dodecagon. The diameter of the  $\text{Al}_{12}$  metal ring is about 9.93 Å. The whole  $\text{Al}_{12}$  cluster is stabilized by 12  $\text{NAP}^-$  and 24  $\text{CH}_3\text{O}^-$ , which can be divided into three layers (Fig. 1b). The peripheral ligands of the middle layer contain six  $\text{NAP}^-$  ligands and six  $\text{CH}_3\text{O}^-$ , which alternately array to form a large outer ring parallel to the  $\text{Al}_{12}$  metal dodecagon (Fig. 1c). The inner part of the middle layer is filled with parallel six  $\text{CH}_3\text{O}^-$ , in which three face up and three faces down. The upper and lower two ligand layers vertical to the  $\text{Al}_{12}$  metal dodecagon are identical and every layer comprises three  $\text{NAP}^-$  and six  $\text{CH}_3\text{O}^-$  (Fig. 1d). Every two methanol molecules are sandwiched between two  $\text{NAP}^-$  ligands. All  $\text{Al}^{3+}$  ions of  $\text{Al}_{12}$  cluster adopt six-coordinated distorted octahedral geometry with six O atoms from 2  $\text{NAP}^-$  and 4  $\text{CH}_3\text{O}^-$ . The  $\text{NAP}^-$  and  $\text{CH}_3\text{O}^-$  respectively adopt  $\mu_2\text{-}\eta^1\text{:}\eta^1$  and  $\mu_2$  connection modes. The Al–O distances and O–Al–O angles are in the range of 1.850–1.946 Å and 77.01–175.27°, respectively.

### Crystal structure of $\text{Al}_{24}$ cluster

Similar to the synthesis of  $\text{Al}_{12}$ , one new  $\text{Al}_{24}$  cluster with the formula

$[\text{Al}_{24}(\text{OH})_{32}(\text{CH}_3\text{O})_{22}(\text{CH}_3\text{OH})_2(\text{NAP})_{12}]\cdot 6\text{Cl}\cdot 2\text{H}_2\text{O}\cdot 2\text{CH}_3\text{OH}$  was obtained by using the solvent of  $\text{CH}_3\text{OH}\text{--}\text{CH}_3\text{CN}$ . It crystallizes in the monoclinic  $P2_1/n$  space group and the asymmetric unit contains half an  $\text{Al}_{24}$  cluster. As shown in Fig. 2a, the  $\text{Al}_{24}$  molecular skeleton is composed of eight  $[\text{Al}_3(\text{OH})(\text{CH}_3\text{O})_3]$  in the truncated positions and six open  $[\text{Al}_8(\text{OH})_4(\text{CH}_3\text{O})_4(\text{NAP})_4]$

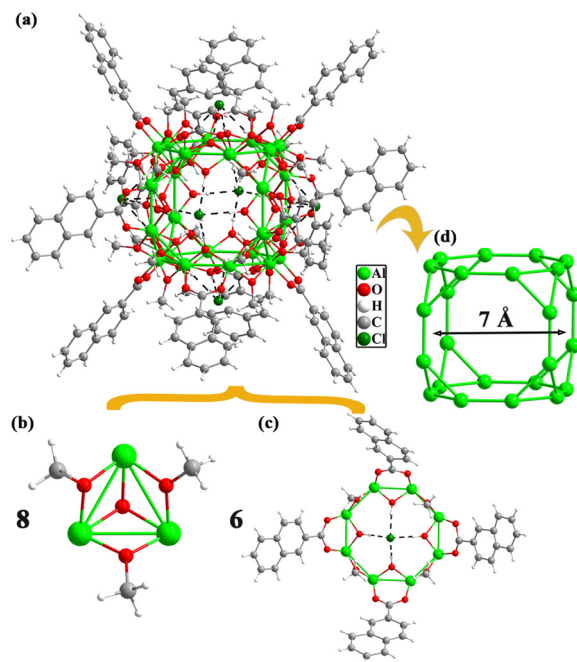


**Fig. 2** (a) Molecular structures of  $\text{Al}_{24}$ . (b) and (c) The  $[\text{Al}_3(\text{OH})(\text{CH}_3\text{O})_3]$  and  $[\text{Al}_8(\text{OH})_4(\text{CH}_3\text{O})_4(\text{NAP})_4]$  building blocks. (d) The 24-nuclearity Al metallic skeleton with a truncated hexahedral geometry (green: Al; red: O; grey: C; dark green: Cl; white: H).

windows. The  $[\text{Al}_3(\text{OH})(\text{CH}_3\text{O})_3]$  building block is coordinated by 3  $\text{CH}_3\text{O}^-$  capped on the Al–Al sides and 1  $\text{OH}^-$  stamped over the centre of the triangle (Fig. 2b). The  $[\text{Al}_8(\text{OH})_4(\text{CH}_3\text{O})_4(\text{NAP})_4]$  consists of four  $\text{NAP}^-$  and  $\text{OH}^-$ , both capped on the interval four sides, and the remaining four sides are fixed by four  $\text{CH}_3\text{O}^-$  (Fig. 2c). The  $\text{Al}_{24}$  is a cation cluster with six free  $\text{Cl}^-$  ions in the centre of octagonal windows bonded to the  $\text{Al}_{24}$  frame by hydrogen-bond interactions, which are formed with four  $\mu_2\text{-OH}^-$  in the interior of the octagon with the  $\text{Cl}\cdots\text{O}$  distances in the range of 3.174–3.302 Å and the  $\text{Cl}\cdots\text{H}\cdots\text{O}$  angles in the range of 161.16–165.06° (Table S4†). This  $\text{Cl}^-$  template interaction is frequently found in the lanthanide clusters, such as  $\text{Dy}_{76}$ ,<sup>41</sup>  $\text{Ln}_{48}$ ,<sup>42–44</sup> and  $\text{Ln}_{15}$ .<sup>45–47</sup> The  $\text{Al}_{24}$  metallic inner features a truncated cube (Fig. 2d) with a small 7 Å diameter, though the total molecular  $\text{Al}_{24}$  cluster with a larger 2.0 nm diameter due to the peripheral big  $\text{NAP}^-$  ligands. The Al–Al interactions are in the range of 2.853(3)–2.976(3) Å.

The Al clusters are also a kind of metallic hydroxide clusters. The simplified Al/O core of  $\text{Al}_{24}$  (Fig. 3c) is composed of the simplified trigonal  $[\text{Al}_3(\text{OH})\text{O}_3]$  and octagonal  $[\text{Al}_8(\text{OH})_8\text{O}_4]$  (Fig. 3a and b) by sharing the sides of the triangles. As depicted in Fig. 3f, the further simplified metal skeleton belongs to one of the 13 Archimedean polyhedra, a truncated cube comprising 8  $\text{Al}_3$  triangles on the truncated positions of the cube (Fig. 3d) and 6  $\text{Al}_8$  octagons on the six faces (Fig. 3e) with the strong Al–Al interactions in the range of 2.850–2.978 Å. This Archimedean polyhedron is rare in the metal nanoclusters, compared with the truncated tetrahedron

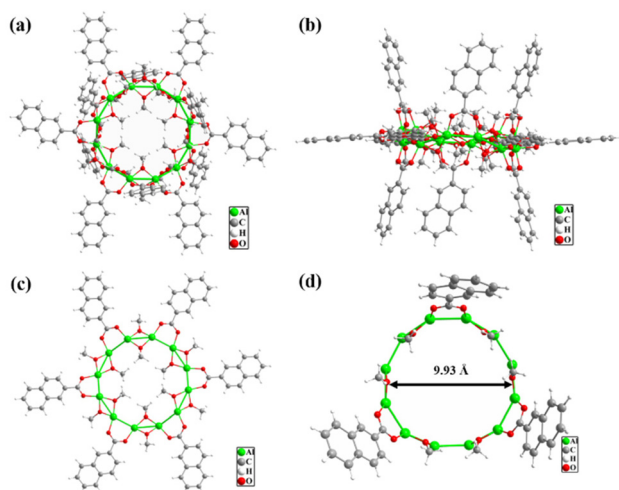


**Fig. 1** (a) and (b) Molecular structures of  $\text{Al}_{12}$  at different view directions. (c) and (d) The ligand arrangement of the middle and upper/lower layers of  $\text{Al}_{12}$  (green: Al; red: O; grey: C; white: H).

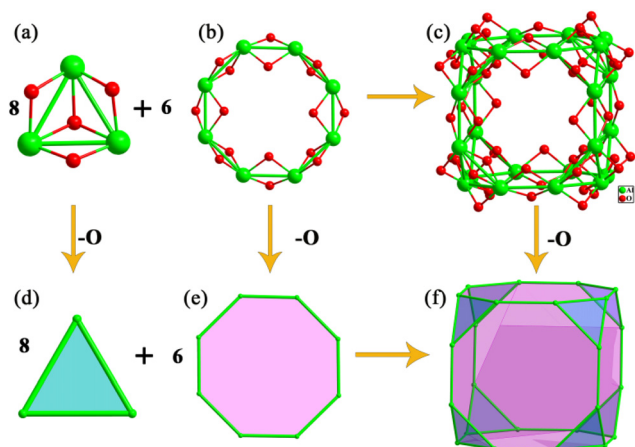


**Fig. 3** (a) and (b)  $[\text{Al}_3(\text{OH})\text{O}_3]$  and  $[\text{Al}_6(\text{OH})_8\text{O}_4]$  building units. (c) The Al/O core of  $\text{Al}_{24}$ . (d) and (e) The simplified  $\text{Al}_3$  triangle (blue) and  $\text{Al}_6$  octagon (purple). (f) The Archimedean polyhedron of  $\text{Al}_{24}$  metallic core (green: Al; red: O).

( $\text{Ag}_{37}$ ),<sup>48</sup> truncated octahedron ( $\text{Co}_{32}$ ),<sup>49</sup> truncated icosahedron ( $\text{Ln}_{60}$ ),<sup>50</sup> whereas some similar  $\text{M}_{24}$  coordination molecular cages with the organic ligands as the linkers have been reported.<sup>51,52</sup>

All  $\text{Al}^{3+}$  ions in the  $\text{Al}_{24}$  cluster adopt six-coordinated distorted octahedral geometry with six O atoms from 3  $\text{OH}^-$ , 1  $\text{NAP}^-$  and 2  $\text{CH}_3\text{O}^-$ . The Al–O contacts and O–Al–O angles are in the range of 1.823–1.987 Å and 74.97–171.3°, respectively. All 12  $\text{NAP}^-$  ligands are situated at the sides of the octagons by adopting a  $\mu_2\text{-}\eta^1\text{:}\eta^1$  connection mode (Fig. S1a†). The 32  $\text{OH}^-$  can be divided into two types, namely, 24  $\mu_2\text{-OH}^-$  is uniformly oriented to the centre of 6 octagon (Fig. S1b†), which are at the opposite positions of every  $\text{NAP}^-$  ligand, whereas the residual 8  $\mu_3\text{-OH}^-$  are capped on the centre of the 8 trigonal  $\text{Al}_3$  building blocks (Fig. S1c†). For the  $\text{CH}_3\text{O}^-$  ligands, all are located on the sharing Al–Al sides of triangular  $\text{Al}_3$  and octagonal  $\text{Al}_6$  building blocks (Fig. S1d†).

### Chemical stability and TG analyses

The stability of  $\text{Al}_{24}$  and  $\text{Al}_{12}$  was measured by immersing their single crystals in water and typical organic solvents. According to the comparison of the experimental and simulated powder X-ray diffraction (PXRD) patterns (Fig. S9†),  $\text{Al}_{24}$  can be kept stable in  $\text{CH}_3\text{OH}$ ,  $\text{EtOH}$ ,  $\text{CH}_3\text{CN}$ , and  $\text{H}_2\text{O}$  at least for a day. For  $\text{Al}_{12}$ , it displays very good stability in  $\text{CH}_3\text{OH}$ ,  $\text{EtOH}$ ,  $\text{CH}_3\text{CN}$ ,  $\text{H}_2\text{O}$ , and DMF for a month (Fig. S10†). The above findings demonstrate that  $\text{Al}_{24}$  and  $\text{Al}_{12}$  exhibit high chemical stability in some solvents and  $\text{H}_2\text{O}$ . As shown in Fig. S8c and S8d,† the experimental IR spectra of  $\text{Al}_{12}$  and  $\text{Al}_{24}$  after immersing their single crystals in water and typical organic solvents were measured to further show their stabilities. Additionally, dry solid samples of  $\text{Al}_{24}$  and  $\text{Al}_{12}$  were used to study the thermal stability under the  $\text{N}_2$  environment from 30 to 800 °C (Fig. S11†). Two  $\text{H}_2\text{O}$  and two  $\text{CH}_3\text{OH}$  molecules were removed from  $\text{Al}_{24}$  during a slight weight loss of 2.33% up to 210 °C

(calcd 2.35%). The mass loss from 210 to 285 °C is due to the departure of 24 coordinated methanol molecules (exp 17.98%, calcd 17.34%). As the temperature increased to 615 °C, the naphthalene rings of the organic  $\text{NAP}^-$  ligands began to break down and the mass fraction of 39.50% was lost (calcd 39.00%). For  $\text{Al}_{12}$ , the first weight loss below 185 °C was ascribed to the removal of four DMF, two  $\text{H}_2\text{O}$ , and two  $\text{CH}_3\text{OH}$  molecules (exp 11.16%, calcd 11.21%). Next, the weight loss of 47.86% from 260 to 440 °C is ascribed to the removal of the naphthalene rings from the  $\text{NAP}^-$  ligands (calcd 47.51%). The third weight loss from 500 to 615 °C corresponds to the decomposition of coordinated methanol molecules.

### Solution behaviours of $\text{Al}_{24}$ and $\text{Al}_{12}$ clusters

The high-resolution electrospray ionization mass spectrometry (ESI-MS) can be used to determine the fragment composition and charge state of the metal clusters.<sup>21,53–60</sup> The negative-mode ESI-MS of  $\text{Al}_{24}$  was investigated by dissolving the crystals in  $\text{CH}_3\text{OH}\text{--}\text{CH}_2\text{Cl}_2$  to analyse its solution stability. As shown in Fig. 4, there are two sets of peaks in the mass-to-charge ( $m/z$ ) ratio ranges of 2000–2100 (1) with  $-2$  charge and 4000–4200 (2) with  $-1$  charge, respectively. For 1 group, the distances between two neighbouring peaks are disparate with 6.51, 7.51, 6.55, 7.47, 7.00, and 7.51 having no uniform variation trend for the seven species (1a–1g). Their compositions, at the positions:  $m/z = 2045.78$ , 2052.20, 2059.79, 2066.22, 2073.79, 2080.79, and 2088.20, can be identified by matching the experimental and simulated isotopic distributions with the corresponding formulas,  $[\text{Al}_{24}(\text{OH})_{34}(\text{CH}_3\text{O})_{26}(\text{NAP})_{11}(\text{H}_2\text{O})_4\text{Cl}_3]^{2-}$ ,  $[\text{Al}_{24}(\text{OH})_{34}(\text{CH}_3\text{O})_{23}(\text{NAP})_{11}(\text{H}_2\text{O})_4\text{Cl}_6]^{2-}$ ,  $[\text{Al}_{24}(\text{OH})_{32}(\text{CH}_3\text{O})_{28}(\text{NAP})_{11}(\text{H}_2\text{O})_4\text{Cl}_3]^{2-}$ ,  $[\text{Al}_{24}(\text{OH})_{32}(\text{CH}_3\text{O})_{25}(\text{NAP})_{11}(\text{H}_2\text{O})_4\text{Cl}_6]^{2-}$ ,  $[\text{Al}_{24}(\text{OH})_{31}(\text{CH}_3\text{O})_{30}(\text{NAP})_{11}(\text{H}_2\text{O})_1\text{Cl}_4\text{H}_2]^{2-}$ ,  $[\text{Al}_{24}(\text{OH})_{31}(\text{CH}_3\text{O})_{31}(\text{NAP})_{11}\text{Cl}_4\text{H}_3]^{2-}$ ,  $[\text{Al}_{24}(\text{OH})_{34}(\text{CH}_3\text{O})_{23}(\text{NAP})_{11}(\text{H}_2\text{O})_6\text{Cl}_7\text{H}_1]^{2-}$  (Table S1†). This set of signals indicates that the metal skeleton of  $\text{Al}_{24}$  cluster is stable in  $\text{CH}_3\text{OH}\text{--}\text{CH}_2\text{Cl}_2$ , whereas the protection groups of  $\text{OH}^-$ ,  $\text{CH}_3\text{O}^-$ , and  $\text{NAP}^-$  exist in the coordination-

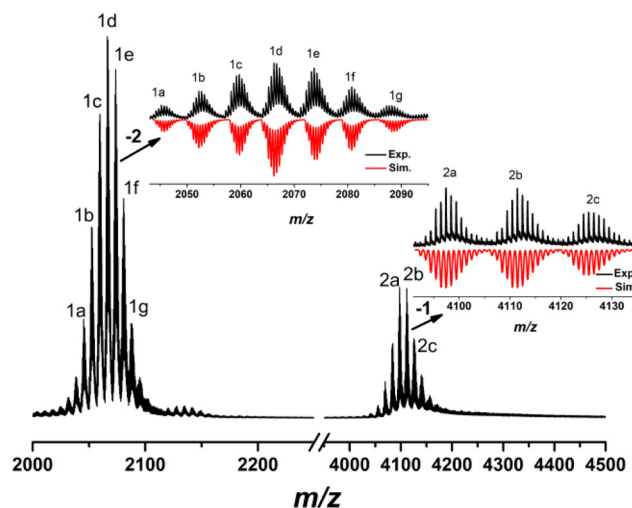


**Fig. 4** The negative-ion ESI-MS of  $\text{Al}_{24}$  in  $\text{CH}_3\text{OH}/\text{CH}_2\text{Cl}_2$ . Inset: the experimental isotopic pattern (block) and simulated (red) data.



disassociation equilibrium. The most dominant peak (1d) with the composition of  $[\text{Al}_{24}(\text{OH})_{32}(\text{CH}_3\text{O})_{25}(\text{NAP})_{11}(\text{H}_2\text{O})_4\text{Cl}_6]^{2-}$  at  $m/z = 2066.22$  is approximate to the parent cluster except for one  $\text{NAP}^-$  replaced with one  $\text{CH}_3\text{O}^-$ . For the 2 groups, **2a–2c** has similar distances of 14.02 corresponding to  $[\text{+CH}_3\text{O}^- \cdot \text{H}_2\text{O} + \text{H}^+]$  with the formulas,  $[\text{Al}_{22}(\text{OH})_{23}(\text{CH}_3\text{O})_{25}(\text{NAP})_{12}(\text{H}_2\text{O})_2\text{Cl}_7]^-$ ,  $[\text{Al}_{22}(\text{OH})_{23}(\text{CH}_3\text{O})_{26}(\text{NAP})_{12}(\text{H}_2\text{O})_1\text{Cl}_7\text{H}_1]^-$ ,  $[\text{Al}_{22}(\text{OH})_{23}(\text{CH}_3\text{O})_{27}(\text{NAP})_{12}\text{Cl}_7\text{H}_2]^-$  at  $m/z = 4097.45$ ,  $4111.47$  and  $4125.48$ , suggesting the presence of the  $\text{Al}_{22}$  fragments in the  $\text{CH}_3\text{OH}$ – $\text{CH}_2\text{Cl}_2$  of  $\text{Al}_{24}$ .

The positive-ion ESI-MS data of  $\text{Al}_{24}$  was also monitored at  $m/z = 500$ – $6000$  (Fig. 5) by dissolving its crystals in  $\text{CH}_3\text{OH}$ – $\text{CH}_2\text{Cl}_2$ . There are four groups (**1a–1f**, **2a–2g**, **3a–3g**, and **4a–4e**) of experimental peaks at  $m/z = 1950$ – $2250$  with +2 charge (see inset in Fig. S2†). By matching the experimental and simulated isotopic distributions, all formulas of fragments are listed in Table S2.† The formulas of **2c–2f** ( $[\text{Al}_{24}(\text{OH})_{32}(\text{CH}_3\text{O})_{24}(\text{NAP})_{12}\text{Cl}_2(\text{H}_2\text{O})_x(\text{CH}_3\text{OH})_{3-x}]^{2+}$ ,  $x = 3, 2, 1, 0$ ), **3a–3f** ( $[\text{Al}_{24}(\text{OH})_{32}(\text{CH}_3\text{O})_{24}(\text{NAP})_{12}\text{Cl}_2(\text{H}_2\text{O})_5(\text{CH}_3\text{CN})_1(\text{CH}_3\text{OH})_1]^{2+}$  (**3a**);  $[\text{Al}_{24}(\text{OH})_{32}(\text{CH}_3\text{O})_{24}(\text{NAP})_{12}\text{Cl}_2(\text{H}_2\text{O})_3(\text{CH}_3\text{CN})_3]^{2+}$  (**3b**);  $[\text{Al}_{24}(\text{OH})_{32}(\text{CH}_3\text{O})_{24}(\text{NAP})_{12}\text{Cl}_2(\text{H}_2\text{O})_2(\text{CH}_3\text{CN})_3(\text{CH}_3\text{OH})_1]^{2+}$  (**3c**);  $[\text{Al}_{24}(\text{OH})_{32}(\text{CH}_3\text{O})_{24}(\text{NAP})_{12}\text{Cl}_3(\text{H}_2\text{O})_4(\text{CH}_3\text{OH})_3\text{H}_1]^{2+}$  (**3d**);  $[\text{Al}_{24}(\text{OH})_{32}(\text{CH}_3\text{O})_{24}(\text{NAP})_{12}\text{Cl}_4(\text{H}_2\text{O})_1(\text{CH}_3\text{OH})_4\text{H}_2]^{2+}$  (**3e**);  $[\text{Al}_{24}(\text{OH})_{32}(\text{CH}_3\text{O})_{24}(\text{NAP})_{12}\text{Cl}_4(\text{CH}_3\text{OH})_5\text{H}_2]^{2+}$  (**3f**)) and **4a–4e** ( $[\text{Al}_{24}(\text{OH})_{32}(\text{CH}_3\text{O})_{24}(\text{NAP})_{12}\text{Cl}_2(\text{H}_2\text{O})_x(\text{CH}_3\text{CN})_4(\text{CH}_3\text{OH})_{6-x}]^{2+}$ ,  $x = 3, 2, 1, 0$ ) are consistent with the molecular formulas of  $\text{Al}_{24}$  ( $[\text{Al}_{24}(\text{OH})_{32}(\text{CH}_3\text{O})_{22}(\text{CH}_3\text{OH})_2(\text{NAP})_{12}] \cdot 6\text{Cl} \cdot 2\text{H}_2\text{O} \cdot 2\text{CH}_3\text{OH}$ ) except for the different number of  $\text{Cl}^-$  and solvent molecules, indicating the stability of total  $\text{Al}_{24}$  structure in  $\text{CH}_3\text{OH}$  and  $\text{CH}_2\text{Cl}_2$  again. Meanwhile, **1b–1f** ( $[\text{Al}_{24}(\text{OH})_{32}(\text{CH}_3\text{O})_{26}(\text{NAP})_{10}\text{Cl}_5(\text{H}_2\text{O})_x(\text{CH}_3\text{OH})_{4-x}\text{H}_3]^{2+}$ ,  $x = 4, 3, 2, 1, 0$ ), **2a** ( $[\text{Al}_{24}(\text{OH})_{32}(\text{CH}_3\text{O})_{26}(\text{NAP})_{10}\text{Cl}_5(\text{H}_2\text{O})_1(\text{CH}_3\text{CN})_2(\text{CH}_3\text{OH})_3\text{H}_3]^{2+}$ ), **2b** ( $[\text{Al}_{24}(\text{OH})_{32}(\text{CH}_3\text{O})_{26}(\text{NAP})_{10}\text{Cl}_5(\text{CH}_3\text{CN})_2(\text{CH}_3\text{OH})_4\text{H}_3]^{2+}$ ) and **3g** ( $[\text{Al}_{24}(\text{OH})_{32}(\text{CH}_3\text{O})_{25}(\text{NAP})_{11}\text{Cl}_4(\text{H}_2\text{O})_3(\text{CH}_3\text{CN})_4(\text{CH}_3\text{OH})_3\text{H}_2]^{2+}$ ) also show the ligand exchange between  $\text{CH}_3\text{O}^-$  and  $\text{NAP}^-$ .

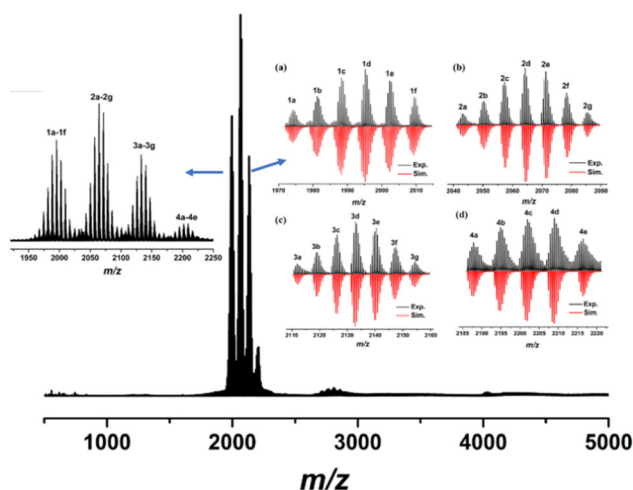


Fig. 5 The positive-ion ESI-MS of  $\text{Al}_{24}$  in  $\text{CH}_3\text{OH}/\text{CH}_2\text{Cl}_2$ . Left inset: the experimental isotopic pattern. Right inset: the experimental isotopic pattern (black) and simulated (red) data.

Similarly, the positive-mode ESI-MS obtained by dissolving the crystals of  $\text{Al}_{12}$  in  $\text{CH}_3\text{OH}$ – $\text{CH}_2\text{Cl}_2$  was also monitored at  $m/z = 1000$ – $6000$  (Fig. 6a). Three groups of experimental peaks at  $m/z = 1950$ – $2020$  (**1a–1j**, +2),  $2100$ – $2160$  (**2a–2f**, +2) and  $2290$ – $2330$  (**3a–3f**, +2) can be clearly assigned by matching the experimental and simulated isotopic distributions (Fig. 6b–d). Two neighbouring peaks of the three groups of experimental data have the same distances with 14.02 corresponding to  $[\text{+CH}_3\text{O}^- \cdot \text{H}_2\text{O} + \text{H}^+]$  and all formulas of fragments are listed in Table S3.† Regrettably, the molecular ion signal was not detected. **1a–1e** assigned to  $[\text{Al}_{12}(\text{CH}_3\text{O})_{17}(\text{NAP})_{17}(\text{H}_2\text{O})_8]^{2+}$  (**1a**);  $[\text{Al}_{12}(\text{CH}_3\text{O})_{16}(\text{NAP})_{18}(\text{H}_2\text{O})_1]^{2+}$  (**1b**);  $[\text{Al}_{12}(\text{CH}_3\text{O})_{17}(\text{NAP})_{18}\text{H}_1]^{2+}$  (**1c**);  $[\text{Al}_{12}(\text{CH}_3\text{O})_{20}(\text{NAP})_{17}(\text{H}_2\text{O})_5\text{H}_3]^{2+}$  (**1d**);  $[\text{Al}_{12}(\text{CH}_3\text{O})_{21}(\text{NAP})_{17}(\text{H}_2\text{O})_4\text{H}_4]^{2+}$  (**1e**), and **2c–2f** assigned to  $[\text{Al}_{12}(\text{CH}_3\text{O})_{14}(\text{NAP})_{20}(\text{H}_2\text{O})_5]^{2+}$  (**2c**);  $[\text{Al}_{12}(\text{CH}_3\text{O})_{15}(\text{NAP})_{20}(\text{H}_2\text{O})_4\text{H}_1]^{2+}$  (**2d**);  $[\text{Al}_{12}(\text{CH}_3\text{O})_{16}(\text{NAP})_{20}(\text{H}_2\text{O})_3\text{H}_2]^{2+}$  (**2e**);  $[\text{Al}_{12}(\text{CH}_3\text{O})_{17}(\text{NAP})_{20}(\text{H}_2\text{O})_2\text{H}_3]^{2+}$  (**2f**) coincide with the metallic core of  $\text{Al}_{12}$  whereas the numbers of  $\text{CH}_3\text{O}^-$  and  $\text{NAP}^-$  are different with the molecular formulas, indicating the occurrence of ligand exchange between  $\text{CH}_3\text{O}^-$ ,  $\text{NAP}^-$  and  $\text{H}_2\text{O}$ . **1f–1i** assigned to  $[\text{Al}_{11}(\text{CH}_3\text{O})_{12}(\text{NAP})_{19}(\text{H}_2\text{O})_3]^{2+}$ ,  $[\text{Al}_{11}(\text{CH}_3\text{O})_{13}(\text{NAP})_{19}(\text{H}_2\text{O})_2\text{H}_1]^{2+}$ ,  $[\text{Al}_{11}(\text{CH}_3\text{O})_{14}(\text{NAP})_{19}(\text{H}_2\text{O})_1\text{H}_2]^{2+}$ , and  $[\text{Al}_{11}(\text{CH}_3\text{O})_{15}(\text{NAP})_{19}\text{H}_3]^{2+}$  lost a metal ion compared with  $\text{Al}_{12}$  and **1j** assigned to  $[\text{Al}_{10}(\text{CH}_3\text{O})_8(\text{NAP})_{20}(\text{H}_2\text{O})_5]^{2+}$  has two fewer metal ions than  $\text{Al}_{12}$ . Interestingly, the fragments of **2a–2b** with the corresponding attribution of  $[\text{Al}_{13}(\text{CH}_3\text{O})_{20}(\text{NAP})_{19}(\text{H}_2\text{O})_1\text{H}_2]^{2+}$  and  $[\text{Al}_{13}(\text{CH}_3\text{O})_{21}(\text{NAP})_{19}\text{H}_3]^{2+}$ , and **3a–3f** with the corresponding attribution of  $[\text{Al}_{14}(\text{CH}_3\text{O})_{20}(\text{NAP})_{20}(\text{H}_2\text{O})_9]^{2+}$ ,  $[\text{Al}_{14}(\text{CH}_3\text{O})_{21}(\text{NAP})_{20}(\text{H}_2\text{O})_8\text{H}_1]^{2+}$ ,  $[\text{Al}_{14}(\text{CH}_3\text{O})_{22}(\text{NAP})_{20}(\text{H}_2\text{O})_7\text{H}_2]^{2+}$ ,  $[\text{Al}_{14}(\text{CH}_3\text{O})_{23}(\text{NAP})_{20}(\text{H}_2\text{O})_6\text{H}_3]^{2+}$ ,  $[\text{Al}_{14}(\text{CH}_3\text{O})_{24}(\text{NAP})_{20}(\text{H}_2\text{O})_5\text{H}_4]^{2+}$ ,  $[\text{Al}_{14}(\text{CH}_3\text{O})_{25}$

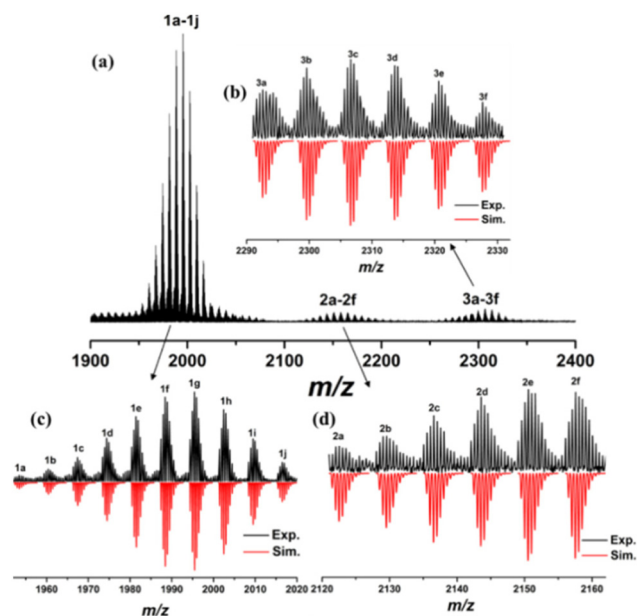


Fig. 6 (a) The positive-ion ESI-MS of  $\text{Al}_{12}$  in  $\text{CH}_3\text{OH}/\text{CH}_2\text{Cl}_2$ . The experimental isotopic pattern (black) and simulated (red) data for 1 group (c), 2 group (d), and 3 group (b).

(NAP)<sub>20</sub>(H<sub>2</sub>O)<sub>4</sub>H<sub>5</sub>]<sup>2+</sup> display the increase of a and two Al<sup>3+</sup> ions for Al<sub>12</sub>. The above analysis result indicates that the metal skeleton of the Al<sub>12</sub> cluster can be partly stable in CH<sub>3</sub>OH and CH<sub>2</sub>Cl<sub>2</sub>, while some fragments with adjacent nuclear numbers, *e.g.*, Al<sub>10</sub>, Al<sub>11</sub>, Al<sub>13</sub>, Al<sub>14</sub> exist in CH<sub>3</sub>OH and CH<sub>2</sub>Cl<sub>2</sub>. Alternatively, the number of CH<sub>3</sub>O<sup>−</sup> is less than the theoretical 24, whereas that of NAP<sup>−</sup> is more. Thus, we surmise that NAP<sup>−</sup> firstly coordinated with Al<sup>3+</sup> ions in the assembly process of Al<sub>12</sub>, and was later replaced by CH<sub>3</sub>O<sup>−</sup>. Besides, the negative-ion ESI-MS data of Al<sub>12</sub> obtained by dissolving its crystals in CH<sub>3</sub>OH–CH<sub>2</sub>Cl<sub>2</sub> was monitored at *m/z* = 500–6000 (Fig. S2†). Only a small fragment peak at *m/z* = 863.15 was detected at *m/z* = 500–6000 and there are no more pieces of information.

### UV-Vis spectra and photocurrent measurements of Al<sub>24</sub> and Al<sub>12</sub>

The solid-state ultraviolet-visible absorption spectra (UV-Vis) of HNAP, Al<sub>24</sub>, and Al<sub>12</sub> were recorded at room temperature. As shown in Fig. S3a and S3b,† the HNAP ligand exhibits absorption at 210 nm, whereas Al<sub>24</sub> and Al<sub>12</sub> have a similar broad absorption band at 250–400 nm. The red-shifted phenomenon may be caused by Al-perturbed  $\pi \rightarrow \pi^*$  transition of the ligand.<sup>61</sup> The band gaps (*E<sub>g</sub>*) of Al<sub>24</sub> and Al<sub>12</sub> are 3.48 and 3.44 eV calculated based on the Kubelka–Munk function, respectively (Fig. S4†),<sup>62</sup> which are much smaller than 9 eV of Al<sub>2</sub>O<sub>3</sub>.<sup>63</sup> This reveals that the aggregation of aluminum ions into aluminum-oxo clusters affects the band gap structure, including the widening of the absorption edge and the narrowing of the band gap.

The photocurrent responses of Al<sub>24</sub> and Al<sub>12</sub> under LED light were further examined by the typical three-electrode system. The working electrode was indium tin oxide (ITO) glass, the auxiliary electrode was platinum wire, and the reference electrode was Ag/AgCl, maintaining the bias voltage of 0.6 V in the meantime. As shown in Fig. 7, upon on–off cycling exposure with LED light ( $\lambda$  = 365 nm and 420 nm; 10 s intervals; 50 W), obvious photocurrent reactions were observed, and the photocurrent densities exhibit a promptly rising or fast falling under light irradiation or no irradiation conditions. This indicates that Al<sub>12</sub> and Al<sub>24</sub> both have fast response speeds to LED light. No matter whether the irradiations wavelengths are at 420 nm or 365 nm, Al<sub>12</sub> generates higher photocurrent values than these of Al<sub>24</sub>, which demonstrates that more efficient generation and separation of photoinduced electron/hole pairs were observed in ITO electrodes of Al<sub>12</sub> under the LED light. This could be explained on the basis of the lower band gap of Al<sub>12</sub> at 3.44 eV.<sup>64</sup> The above experimental results exhibiting Al<sub>12</sub> and Al<sub>24</sub> are a kind of potential photoelectric materials.

### Luminescence properties of Al<sub>24</sub> and Al<sub>12</sub>

At room temperature, the solid-state luminescence properties of HNAP, Al<sub>24</sub>, and Al<sub>12</sub> were observed (Fig. S5†). The maximum emission of HNAP was at 372 nm under a maximum excitation wavelength of 319 nm (Fig. S5a and 5b†), which originated from the intramolecular  $\pi-\pi^*$  transition of the HNAP organic ligand. As illustrated in Fig. S5c and 5d,† the Al<sub>24</sub> cluster exhibits the ligand-centered blue fluorescence

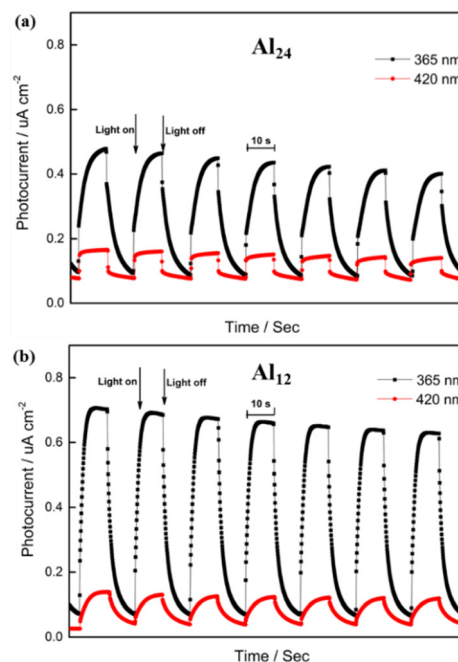


Fig. 7 Transient photocurrent responses of Al<sub>24</sub> (a) and Al<sub>12</sub> (b).

with emission at 374 nm under 319 nm excitation. A similar blue fluorescence from ligand-centered emission is also observed in Al<sub>12</sub> with the maximum emission wavelength at 389 nm under 352 nm excitation (Fig. S5e and 5f†).

To determine their potential applications as optical thermometers, the operating range for the temperature-dependent luminescence spectra of Al<sub>24</sub> and Al<sub>12</sub> was from 300 to 120 K. The temperature was changed from 300 K to 120 K, but the emission location of the Al<sub>24</sub> cluster remained fixed at *x* = 0.15 and *y* = 0.06 in the CIE space (Fig. S6a and Table S5†) in the blue-light region (Fig. 8a). Furthermore, the emission position

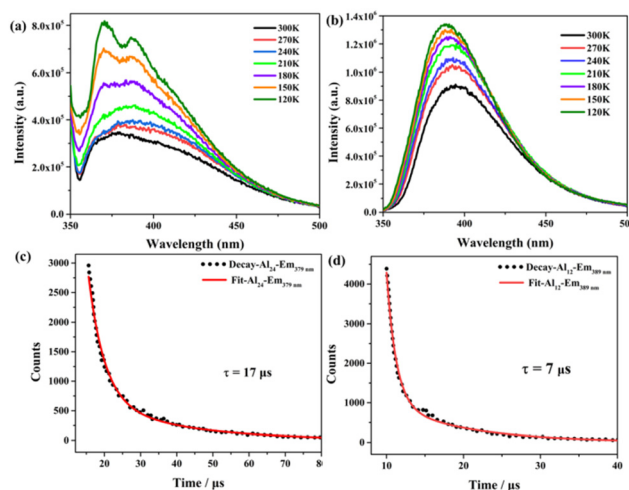


Fig. 8 The temperature-dependent luminescence spectra of Al<sub>24</sub> (a) and Al<sub>12</sub> (b) from 300 K to 120 K. Luminescence lifetimes of Al<sub>24</sub> (c,  $\lambda_{\text{em}}$  = 379 nm) and Al<sub>12</sub> (d,  $\lambda_{\text{em}}$  = 389 nm) at room temperature.

of  $\text{Al}_{12}$  is slightly blue-shifted from 394.5 nm to 387.5 nm, as the temperature drops from 300 K to 120 K (Fig. 8b) while the CIE coordinates of the emission positions change from  $x = 0.16, y = 0.05$  to  $x = 0.17, y = 0.07$  (Fig. S6b and Table S5†). The probable reason is the restricted rotation of ligands in  $\text{Al}_{12}$  at lower temperatures. In addition, the emission intensity of  $\text{Al}_{24}$  and  $\text{Al}_{12}$  gradually increased with decreasing temperature on account of the reduction of non-radiative decay.

The time-resolved decay curves of the  $\text{Al}_{24}$  and  $\text{Al}_{12}$  clusters were recorded at room temperature, and their fitting results show the double exponential functions. The lifetimes of  $\text{Al}_{24}$  and  $\text{Al}_{12}$  are 17  $\mu\text{s}$  ( $\lambda_{\text{em}} = 379$  nm;  $\tau_1 = 4.44$ , 37%;  $\tau_2 = 24.4$ , 63%; Fig. 8c) and 7  $\mu\text{s}$  ( $\lambda_{\text{em}} = 389$  nm;  $\tau_1 = 1.26$ , 35%;  $\tau_2 = 10.26$ , 65%; Fig. 8d). The absolute solid-state quantum yields of the  $\text{Al}_{24}$  and  $\text{Al}_{12}$  are 25.11% and 18.42%, respectively. The different luminescence behaviours of  $\text{Al}_{24}$  and  $\text{Al}_{12}$  can be attributed to the different ligand environments in the crystal-line structures, generating the different constraints on the rotation of the  $\text{NAP}^-$  ligands.

## Conclusions

In summary, we synthesized an  $\text{Al}_{12}$  molecular ring and a rare  $\text{Al}_{24}$  metallocage based on the  $\text{NAP}^-$  ligand obtained by modulating the solvent in a simple one-pot solvothermal reaction. The  $\text{Al}_{12}$  is a dodecagonal molecular ring and the  $\text{Al}_{24}$  metallocage can be seen as a truncated cube composed of eight  $\text{Al}_3$  triangles and six  $\text{Al}_8$  octagons formed by sharing vertical  $\text{Al}^{3+}$  ions, realizing the complete change of Al-oxo skeletons. Interestingly, the  $\text{Al}_{12}$  and  $\text{Al}_{24}$  clusters exhibited the photo-current-generating capacity and luminescent behaviour, indicating that the Al clusters are potentially photocatalytic and luminescent materials.

## Conflicts of interest

There are no conflicts to declare.

## Acknowledgements

This work was supported by the National Natural Science Foundation of China (no. 22101148) and the Natural Science Foundation of Shandong Province (no. ZR2021QB008).

## References

- 1 S. Schein and J. M. Gayed, Fourth class of convex equilateral polyhedron with polyhedral symmetry related to fullerenes and viruses, *Proc. Natl. Acad. Sci. U. S. A.*, 2014, **111**, 2920–2925.
- 2 C. Stump, AI aids intuition in mathematical discovery, *Nature*, 2021, **600**, 44–45.
- 3 I. Severcan, C. Geary, A. Chworos, N. Voss, E. Jacovetty and L. Jaeger, A polyhedron made of tRNAs, *Nat. Chem.*, 2010, **2**, 772–779.
- 4 R. Twarock and A. Luque, Structural puzzles in virology solved with an overarching icosahedral design principle, *Nat. Commun.*, 2019, **10**, 4414.
- 5 R. Iinuma, Y. Ke, R. Jungmann, T. Schlichthaerle, J. B. Woehrstein and P. Yin, Polyhedra Self-Assembled from DNA Tripods and Characterized with 3D DNA-PAINT, *Science*, 2014, **344**, 65–69.
- 6 J.-P. Lang, Q.-F. Xu, Z.-N. Chen and B. F. Abrahams, Assembly of a Supramolecular Cube,  $[(\text{Cp}^*\text{WS}_3\text{Cu}_3)_8\text{Cl}_8(\text{CN})_{12}\text{Li}_4]$  from a Preformed Incomplete Cubane-like Compound  $[\text{PPh}_4][\text{Cp}^*\text{WS}_3(\text{CuCN})_3]$ , *J. Am. Chem. Soc.*, 2003, **125**, 12682–12683.
- 7 S. R. Seidel and P. J. Stang, High-Symmetry Coordination Cages via Self-Assembly, *Acc. Chem. Res.*, 2002, **35**, 972–983.
- 8 A. V. Virovets, E. Peresypkina and M. Scheer, Structural Chemistry of Giant Metal Based Supramolecules, *Chem. Rev.*, 2021, **121**, 14485–14554.
- 9 D. Fujita, Y. Ueda, S. Sato, N. Mizuno, T. Kumasaka and M. Fujita, Self-assembly of tetravalent Goldberg polyhedra from 144 small components, *Nature*, 2016, **540**, 563–566.
- 10 X. Z. Li, C. B. Tian and Q. F. Sun, Coordination-Directed Self-Assembly of Functional Polynuclear Lanthanide Supramolecular Architectures, *Chem. Rev.*, 2022, **122**, 6374–6458.
- 11 S. J. Bao, Z. M. Xu, T. C. Yu, Y. L. Song, H. Wang, Z. Niu, X. Li, B. F. Abrahams, P. Braunstein and J. P. Lang, Flexible Vertex Engineers the Controlled Assembly of Distorted Supramolecular Tetrahedral and Octahedral Cages, *Research*, 2022, **2022**, 9819343.
- 12 S. J. Bao, Z. M. Xu, Y. Ju, Y. L. Song, H. Wang, Z. Niu, X. Li, P. Braunstein and J. P. Lang, The Covalent and Coordination Co-Driven Assembly of Supramolecular Octahedral Cages with Controllable Degree of Distortion, *J. Am. Chem. Soc.*, 2020, **142**, 13356–13361.
- 13 Z. H. Wei, C. Y. Ni, H. X. Li, Z. G. Ren, Z. R. Sun and J. P. Lang,  $[\text{PyH}][\{\text{TpMo}(\mu_3\text{-S})_4\text{Cu}_3\}_4(\mu_{12}\text{-I})]$ : a unique tetracubane cluster derived from the S-S bond cleavage and the iodide template effects and its enhanced NLO performances, *Chem. Commun.*, 2013, **49**, 4836–4838.
- 14 L. Yang, X.-Y. Wang, X.-Y. Tang, M.-Y. Wang, C.-Y. Ni, H. Yu, Y.-L. Song, B. F. Abrahams and J.-P. Lang, Temperature-dependent chloride-mediated access to atom-precise silver thiolate nanoclusters, *Sci. China: Chem.*, 2022, **65**, 1094–1099.
- 15 H. W. Kroto, J. R. Heath, S. C. O'Brien, R. F. Curl and R. E. Smalley,  $\text{C}_{60}$ : Buckminsterfullerene, *Nature*, 1985, **318**, 162–163.
- 16 J. Spandl, I. Brüdgam and H. Hartl, Solvothermal Synthesis of a 24-Nuclear, Cube-Shaped Squarato-oxovanadium(IV) Framework:  $[\text{N}(\text{nBu})_4]_8[\text{V}_{24}\text{O}_{24}(\text{C}_4\text{O}_4)_{12}(\text{OCH}_3)_{32}]$ , *Angew. Chem., Int. Ed.*, 2001, **40**, 4018–4020.

- 17 Y. Bi, S. Du and W. Liao, Thiacalixarene-based nanoscale polyhedral coordination cages, *Coord. Chem. Rev.*, 2014, **276**, 61–72.
- 18 S. P. Argent, A. Greenaway, M. d. C. Gimenez-Lopez, W. Lewis, H. Nowell, A. N. Khlobystov, A. J. Blake, N. R. Champness and M. Schroder, High-nuclearity metal-organic nanospheres: a  $\text{Cd}_{66}$  ball, *J. Am. Chem. Soc.*, 2012, **134**, 55–58.
- 19 J. Lin, N. Li, S. Yang, M. Jia, J. Liu, X. M. Li, L. An, Q. Tian, L. Z. Dong and Y. Q. Lan, Self-Assembly of Giant  $\text{Mo}_{240}$  Hollow Opening Dodecahedra, *J. Am. Chem. Soc.*, 2020, **142**, 13982–13988.
- 20 N. T. Tran, D. R. Powell and L. F. Dahl, Nanosized  $\text{Pd}_{145}(\text{CO})_x(\text{PET}_3)_{30}$  Containing a Capped Three-Shell 145-Atom Metal-Core Geometry of Pseudo Icosahedral Symmetry, *Angew. Chem., Int. Ed.*, 2000, **39**, 4121–4125.
- 21 Z. Wang, H. F. Su, Y. Z. Tan, S. Schein, S. C. Lin, W. Liu, S. A. Wang, W. G. Wang, C. H. Tung, D. Sun and L. S. Zheng, Assembly of silver Trigons into a buckyball-like  $\text{Ag}_{180}$  nanocage, *Proc. Natl. Acad. Sci. U. S. A.*, 2017, **114**, 12132–12137.
- 22 J. B. Peng, X. J. Kong, Q. C. Zhang, M. Orendac, J. Prokleska, Y. P. Ren, L. S. Long, Z. Zheng and L. S. Zheng, Beauty, symmetry, and magnetocaloric effect—four-shell keplerates with 104 lanthanide atoms, *J. Am. Chem. Soc.*, 2014, **136**, 17938–17941.
- 23 S. L. Heath, P. A. Jordan, I. D. Johnson, G. R. Moore, A. K. Powell and M. Helliwell, Comparative X-ray and  $^{27}\text{Al}$  NMR spectroscopic studies of the speciation of aluminum in aqueous systems:  $\text{Al}(\text{III})$  complexes of  $\text{N}(\text{CH}_2\text{CO}_2\text{H})_2(\text{CH}_2\text{CH}_2\text{OH})$ , *J. Inorg. Biochem.*, 1995, **59**, 785–794.
- 24 S. Abeyasinghe, D. K. Unruh and T. Z. Forbes, Crystallization of Keggin-Type Polyaluminum Species by Supramolecular Interactions with Disulfonate Anions, *Cryst. Growth Des.*, 2012, **12**, 2044–2051.
- 25 W. Wang, K. M. Wentz, S. E. Hayes, D. W. Johnson and D. A. Keszler, Synthesis of the hydroxide cluster  $[\text{Al}_{13}(\mu_3\text{-OH})_6(\mu\text{-OH})_{18}(\text{H}_2\text{O})_{24}]^{15+}$  from an aqueous solution, *Inorg. Chem.*, 2011, **50**, 4683–4685.
- 26 B. L. Fulton, C. K. Perkins, R. H. Mansergh, M. A. Jenkins, V. Gouliouk, M. N. Jackson, J. C. Ramos, N. M. Rogovoy, M. T. Gutierrez-Higgins, S. W. Boettcher, J. F. Conley, D. A. Keszler, J. E. Hutchison and D. W. Johnson, Minerals to Materials: Bulk Synthesis of Aqueous Aluminum Clusters and Their Use as Precursors for Metal Oxide Thin Films, *Chem. Mater.*, 2017, **29**, 7760–7765.
- 27 S. E. Smart, J. Vaughn, I. Pappas and L. Pan, Controlled step-wise isomerization of the Keggin-type  $\text{Al}_{13}$  and determination of the  $\gamma\text{-Al}_{13}$  structure, *Chem. Commun.*, 2013, **49**, 11352–11354.
- 28 L. Allouche, C. Gérardin, T. Loiseau, G. Férey and F. Taulelle,  $\text{Al}_{30}$ : A Giant Aluminum Polycation, *Angew. Chem., Int. Ed.*, 2000, **39**, 511–514.
- 29 K. S. Lokare, N. Frank, B. Braun-Cula, I. Goikoetxea, J. Sauer and C. Limberg, Trapping Aluminum Hydroxide Clusters with Trisilanols during Speciation in Aluminum (III)-Water Systems: Reproducible, Large Scale Access to Molecular Aluminate Models, *Angew. Chem., Int. Ed.*, 2016, **55**, 12325–12329.
- 30 W. Schmitt, E. Baissa, A. Mandel, C. E. Anson and A. K. Powell,  $[\text{Al}_{15}(\mu_3\text{-O})_4(\mu_3\text{-OH})_6(\mu\text{-OH})_{14}(\text{hpdt})_4]^{3-}$ —A New  $\text{Al}_{15}$  Aggregate Which Forms a Supramolecular Zeotype, *Angew. Chem., Int. Ed.*, 2001, **40**, 3577–3581.
- 31 E. A. Cochran, K. N. Woods, D. W. Johnson, C. J. Page and S. W. Boettcher, Unique chemistries of metal-nitrate precursors to form metal-oxide thin films from solution: materials for electronic and energy applications, *J. Mater. Chem. A*, 2019, **7**, 24124–24149.
- 32 Y. J. Liu, Q. H. Li, D. J. Li, X. Z. Zhang, W. H. Fang and J. Zhang, Designable  $\text{Al}_{32}$ -Oxo Clusters with Hydrotalcite-like Structures: Snapshots of Boundary Hydrolysis and Optical Limiting, *Angew. Chem., Int. Ed.*, 2021, **60**, 4849–4854.
- 33 Y. Li, C. Zheng, S. T. Wang, Y. J. Liu, W. H. Fang and J. Zhang, Record Aluminum Molecular Rings for Optical Limiting and Nonlinear Optics, *Angew. Chem., Int. Ed.*, 2022, **61**, e202116563.
- 34 S. T. Wang, Y. J. Liu, C. C. Feng, W. H. Fang and J. Zhang, The largest aluminum molecular rings: Phenol-thermal synthesis, photoluminescence, and optical limiting, *Aggregate*, 2022, e264.
- 35 Y. J. Liu, Y. F. Sun, S. H. Shen, S. T. Wang, Z. H. Liu, W. H. Fang, D. S. Wright and J. Zhang, Water-stable porous  $\text{Al}_{24}$  Archimedean solids for removal of trace iodine, *Nat. Commun.*, 2022, **13**, 6632.
- 36 L. Geng, C. H. Liu, S. T. Wang, W. H. Fang and J. Zhang, Designable Aluminum Molecular Rings: Ring Expansion and Ligand Functionalization, *Angew. Chem., Int. Ed.*, 2020, **59**, 16735–16740.
- 37 X. Z. Zhang, X. F. Wang, W. H. Fang and J. Zhang, Synthesis, Structures, and Fluorescence Properties of Dimeric Aluminum Oxo Clusters, *Inorg. Chem.*, 2021, **60**, 7089–7093.
- 38 O. V. B. Dolomanov, L. J. Bourhis, R. J. Gildea, J. A. K. Howard and H. Puschmann, OLEX2: a complete structure solution, refinement and analysis program, *J. Appl. Crystallogr.*, 2009, **42**, 339–341.
- 39 G. M. Sheldrick, A short history of SHELX, *Acta Crystallogr., Sect. A: Found. Crystallogr.*, 2008, **64**, 112–122.
- 40 A. L. Spek, Structure validation in chemical crystallography, *Acta Crystallogr., Sect. D: Biol. Crystallogr.*, 2009, **65**, 148.
- 41 X. Y. Li, H. F. Su, Q. W. Li, R. Feng, H. Y. Bai, H. Y. Chen, J. Xu and X. H. Bu, A Giant  $\text{Dy}_{76}$  Cluster: A Fused Bi-Nanopillar Structural Model for Lanthanide Clusters, *Angew. Chem., Int. Ed.*, 2019, **58**, 10184–10188.
- 42 M. Wu, F. Jiang, D. Yuan, J. Pang, J. Qian, S. A. Al-Thabaiti and M. Hong, Polymeric double-anion templated  $\text{Er}_{48}$  nanotubes, *Chem. Commun.*, 2014, **50**, 1113–1115.
- 43 F.-S. Guo, Y.-C. Chen, L.-L. Mao, W.-Q. Lin, J.-D. Leng, R. Tarasenko, M. Orendáč, J. Prokleška, V. Sechovský and M.-L. Tong, Anion-Templated Assembly and



- Magnetocaloric Properties of a Nanoscale  $\{\text{Gd}_{38}\}$  Cage versus a  $\{\text{Gd}_{48}\}$  Barrel, *Chem. – Eur. J.*, 2013, **19**, 14876–14885.
- 44 X.-Y. Li, Y. Jing, J. Zheng, H. Ding, Q. Li, M.-H. Yu and X.-H. Bu, Two Luminescent High-Nuclearity Lanthanide Clusters  $\text{Ln}_{48}$  ( $\text{Ln} = \text{Eu}$  and  $\text{Tb}$ ) with a Nanopillar Structure, *Cryst. Growth Des.*, 2020, **20**, 5294–5301.
  - 45 R. Wang, Z. Zheng, T. Jin and R. J. Staples, Coordination Chemistry of Lanthanides at “High” pH: Synthesis and Structure of the Pentadecanuclear Complex of Europium (III) with Tyrosine, *Angew. Chem.*, 1999, **111**, 1929–1932.
  - 46 W. Huang, Z. Zhang, Y. Wu, W. Chen, D. A. Rotsch, L. Messerle and Z. Zheng, A systematic study of halide-template effects in the assembly of lanthanide hydroxide cluster complexes with histidine, *Inorg. Chem. Front.*, 2021, **8**, 26–34.
  - 47 D. T. Thielemann, A. T. Wagner, Y. Lan, P. Ona-Burgos, I. Fernandez, E. S. Rosch, D. K. Kolmel, A. K. Powell, S. Brase and P. W. Roesky, Peptoid-ligated pentadecanuclear yttrium and dysprosium hydroxy clusters, *Chem. – Eur. J.*, 2015, **21**, 2813–2820.
  - 48 X. Y. Li, H. F. Su, K. Yu, Y. Z. Tan, X. P. Wang, Y. Q. Zhao, D. Sun and L. S. Zheng, A platonic solid templating Archimedean solid: an unprecedented nanometre-sized  $\text{Ag}_{37}$  cluster, *Nanoscale*, 2015, **7**, 8284–8288.
  - 49 Y. Bi, X.-T. Wang, W. Liao, X. Wang, X. Wang, H. Zhang and S. Gao, A  $\{\text{Co}_{32}\}$  Nanosphere Supported by p-tert-Butylthiacalix[4]arene, *J. Am. Chem. Soc.*, 2009, **131**, 11650–11651.
  - 50 X.-J. Kong, Y. Wu, L.-S. Long, L.-S. Zheng and Z. Zheng, A Chiral 60-Metal Sodalite Cage Featuring 24 Vertex-Sharing  $[\text{Er}_4(\mu_3\text{-OH})_4]$  Cubanes, *J. Am. Chem. Soc.*, 2009, **131**, 6918–6919.
  - 51 Y. Domoto, M. Abe and M. Fujita, A Highly Entangled  $(\text{M}_3\text{L}_2)_8$  Truncated Cube from the Anion-Controlled Oligomerization of a pi-Coordinated  $\text{M}_3\text{L}_2$  Subunit, *J. Am. Chem. Soc.*, 2021, **143**, 8578–8582.
  - 52 K. Su, M. Wu, D. Yuan and M. Hong, Interconvertible vanadium-seamed hexameric pyrogallol[4]arene nanocapsules, *Nat. Commun.*, 2018, **9**, 4941.
  - 53 L. Tang, A. Ma, C. Zhang, X. Liu, R. Jin and S. Wang, Total Structure of Bimetallic Core-Shell  $[\text{Au}_{42}\text{Cd}_{40}(\text{SR})_{52}]^{2-}$  Nanocluster and Its Implications, *Angew. Chem., Int. Ed.*, 2021, **60**, 17969–17973.
  - 54 S. Lee, M. S. Bootharaju, G. Deng, S. Malola, W. Baek, H. Hakkinen, N. Zheng and T. Hyeon,  $[\text{Cu}_{32}(\text{PET})_{24}\text{H}_8\text{Cl}_2](\text{PPh}_4)_2$ : A Copper Hydride Nanocluster with a Bisquare Antiprismatic Core, *J. Am. Chem. Soc.*, 2020, **142**, 13974–13981.
  - 55 J. J. Li, Z. J. Guan, Z. Lei, F. Hu and Q. M. Wang, Same Magic Number but Different Arrangement: Alkynyl-Protected  $\text{Au}_{25}$  with  $\text{D}_3$  Symmetry, *Angew. Chem., Int. Ed.*, 2019, **58**, 1083–1087.
  - 56 Y.-K. Deng, H.-F. Su, J.-H. Xu, W.-G. Wang, M. Kurmoo, S.-C. Lin, Y.-Z. Tan, J. Jia, D. Sun and L.-S. Zheng, Hierarchical Assembly of a  $\{\text{Mn}^{\text{II}}_{15}\text{Mn}^{\text{III}}_4\}$  Brucite Disc: Step-by-Step Formation and Ferrimagnetism, *J. Am. Chem. Soc.*, 2016, **138**, 1328–1334.
  - 57 X. Y. Li, H. F. Su, M. Kurmoo, C. H. Tung, D. Sun and L. S. Zheng, Structure, solution assembly, and electroconductivity of nanosized argento-organic-cluster/framework templated by chromate, *Nanoscale*, 2017, **9**, 5305–5314.
  - 58 X. Y. Li, H. F. Su, Q. W. Li, R. Feng, H. Y. Bai, H. Y. Chen, J. Xu and X. H. Bu, A Giant  $\text{Dy}_{76}$  Cluster: A Fused Bi-Nanopillar Structural Model for Lanthanide Clusters, *Angew. Chem., Int. Ed.*, 2019, **58**, 10184–10188.
  - 59 H. Zheng, M.-H. Du, S.-C. Lin, Z.-C. Tang, X.-J. Kong, L.-S. Long and L.-S. Zheng, Assembly of a Wheel-Like  $\text{Eu}_{24}\text{Ti}_8$  Cluster under the Guidance of High-Resolution Electrospray Ionization Mass Spectrometry, *Angew. Chem., Int. Ed.*, 2018, **57**, 10976–10979.
  - 60 Y.-Y. Zhang, D.-S. Zhang, T. Li, M. Kurmoo and M.-H. Zeng, In Situ Metal-Assisted Ligand Modification Induces  $\text{Mn}_4$  Cluster-to-Cluster Transformation: A Crystallography, Mass Spectrometry, and DFT Study, *Chem. – Eur. J.*, 2020, **26**, 721–728.
  - 61 J. H. Weber, Complexes of pyrrole-derivative ligands. I., Planar nickel(II) complexes with tetradentate ligands, *Inorg. Chem.*, 1967, **6**, 258–262.
  - 62 Y. Mu, D. Wang, X.-D. Meng, J. Pan, S.-D. Han and Z.-Z. Xue, Construction of Iodoargentates with Diverse Architectures: Template Syntheses, Structures, and Photocatalytic Properties, *Cryst. Growth Des.*, 2020, **20**, 1130–1138.
  - 63 K. Matsunaga, T. Mizoguchi, A. Nakamura, T. Yamamoto and Y. Ikuhara, Formation of titanium-solute clusters in alumina: A first-principles study, *Appl. Phys. Lett.*, 2004, **84**, 4795–4797.
  - 64 A. Kongkanand, K. Tvrđy, K. Takechi, M. Kuno and P. V. Kamat, Quantum Dot Solar Cells. Tuning Photoresponse through Size and Shape Control of  $\text{CdSe-TiO}_2$  Architecture, *J. Am. Chem. Soc.*, 2008, **130**, 4007–4015.